

1 **Barrier layer design reduces top electrode ion migration in**
2 **perovskite solar cells**

3

4 *Saivineeth Penukula¹, Megh N Khanal², Mohin Sharma³, Mritunjaya Parashar³, Ross A.*
5 *Kerner⁴, Min Chen⁴, Melissa A. Davis⁴, Rafikul Ali Saha⁵, Eduardo Solano⁶, Maarten B.J.*
6 *Roeffaers⁵, Joseph J. Berry^{4,7,8}, Joseph M. Luther^{4,8}, Julian A. Steele^{9,10}, Axel Palmstrom⁴,*
7 *Vincent R Whiteside², Bibhudutta Rout³, Ian R. Sellers², Nicholas Rolston^{1*}*

8

9 ¹*Renewable Energy Materials and Devices Lab, School of Electrical, Computer and Energy*
10 *Engineering (ECEE), Arizona State University, Tempe, Arizona 85281, USA*

11 ²*Department of Electrical Engineering, 230 Davis Hall, University at Buffalo SUNY, Buffalo,*
12 *New York 14260, USA*

13 ³*Department of Physics, Ion Beam Laboratory, University of North Texas, Denton, Texas*
14 *76203, USA*

15 ⁴*National Renewable Energy Laboratory, Golden, Colorado 80309, USA*

16 ⁵*cMACS, Department of Microbial and Molecular Systems, KU Leuven, Celestijnenlaan 200F,*
17 *3001 Heverlee, Belgium*

18 ⁶*NCD-SWEET Beamline, ALBA Synchrotron Light Source, 08290 Cerdanyola del Vallès,*
19 *Barcelona, Spain*

20 ⁷*Department of Physics, University of Colorado Boulder, Boulder, Colorado 80309, USA*

21 ⁸*Renewable and Sustainable Energy Institute, University of Colorado Boulder, Boulder,*
22 *Colorado 80309, USA*

23 ⁹*Australian Institute of Bioengineering and Nanotechnology, The University of Queensland, St*
24 *Lucia, QLD 4072, Australia*

25 ¹⁰*School of Mathematics and Physics, The University of Queensland, Brisbane, QLD 4072,*
26 *Australia*

27 *Corresponding author and lead contact:

28 Prof. Nicholas Rolston

29 Renewable Energy Materials and Devices Lab,

30 School of Electrical, Computer, and Energy Engineering (ECEE),

31 Arizona State University,

32 Tempe, AZ, USA

33 e-mail: nicholas.rolston@asu.edu

34 ORCID: orcid.org/0000-0001-8093-1689

35 **Summary**

36 We report on an examination of mobile ion concentration (N_o) in perovskite solar cells (PSCs)
37 as a function of temperature and device architecture. We find that lower initial N_o is correlated
38 to devices with higher thermal performance through in-situ measurements up to 450K. Changes
39 in N_o are observed upon thermal aging and are impacted by the changes made at the electron
40 collecting interface. We examine the extent to which various top electrode materials (Ag, Au,
41 carbon) impact N_o as well as the effects of tin oxide (SnO_2) or an ozone-nucleated SnO_2 (O_3 -
42 SnO_2) barrier layer between the ETL and top electrode. Upon thermal aging, we confirm the
43 involvement of Ag ion diffusion through the ETL dependent on the device details. We are able
44 to quantify the degree to which Ag ions migrate or are blocked from migrating into the
45 underlying device layers in the PSC stack. X-ray scattering shows improved suppression of the
46 degradation products formed in the bulk of the perovskite when a blocking layer, particularly
47 the O_3 - SnO_2 is employed.

48 **Keywords:** mobile ions, tin oxide, activation energy, reliability, diffusion, spectroscopy, X-ray
49 scattering, degradation, aging

50 **Broader Context**

51 Ion migration is one of the important factors that affect the operational lifetime and stability of
52 perovskite solar cells (PSCs). Even though different methodologies have been employed to
53 show the effects of ion migration, the techniques are varied and often qualitative. Furthermore,
54 there is no simple, quantitative method that provides a consistent correlation to the stability of
55 PSCs. This work shows that mobile ion concentration (N_o) can be correlated to PSC stability
56 in state-of-the-art devices. N_o is a metric that can serve as a consistent and straightforward
57 approach to quantify ion migration-related degradation modes on PSC stability.

58

59

60

61

62

63

64

65

66

67

68

69

70 **Introduction**

71 Metal-halide perovskite (MHP) solar cells have achieved significant commercial
72 interest in the renewable energy market based on rapid efficiency improvements(1,2) achieving
73 lab efficiencies of 26.7%.(3) Additional advantages include the use of earth-abundant
74 precursors, affordable manufacturing, and tunability of optoelectronic properties.(4–7)
75 However, the ion migration and chemical reactions observed under the influence of
76 environmental stressors such as heat and light are a concern.(8,9) The pace of perovskite solar
77 cell (PSC) advances has made it difficult for field testing studies to keep pace with reports in
78 excess of 10000 h limited to older devices and architectures.(10) Limited field lifetimes (< 1
79 year) for the majority of PSC modules tested by the perovskite PV accelerator for
80 commercializing technologies (PACT)(11) indicates this challenge of demonstrating sufficient
81 reliability to bring PSCs to market. This rapid development cycle creates a need for more rapid
82 testing methods and metrics as well as mechanistic insight related to stability and reliability
83 issues in PSCs. Of the variety of mechanisms believed to be responsible for a change in
84 efficiency in operation, ion migration is postulated to be a primary cause of this degradation
85 via phase separation and reactions with charge transport layers. While these correlations have
86 been identified, the mechanism that ultimately leads to electronic losses and irreversible
87 corrosion of electrodes is still being revealed.(12–15) Here we undertake studies to examine
88 changes in mobile species and how these relate to device stability. Specifically, we use our
89 previously reported measurement approach to study the change in mobile ion concentration
90 (N_o). These measurements are sensitive to mobile charges induced directly or indirectly by
91 mobile ions and chemical reactions, providing a basis from which to see how these changes as
92 devices are stressed, and subsequently examine the specific origins of degradation for a given
93 device architecture.

94 Recent work has shown that the top metal electrodes in PSCs spontaneously react(15)
95 or can react under electrochemical(16,17) or photochemical stress.(18) One strategy to prevent
96 reactions and the formation of mobile ions is to employ a physical barrier layer.(19) However,
97 this barrier layer must be of very high quality (i.e. chemically stable and pinhole-free) to be
98 effective. The best barrier layers are often created by atomic layer deposition (ALD) of metal
99 oxides such as SnO_2 on top of the fullerene-based electron transport layer (ETL) in the p-i-n
100 structure of PSCs.(20) The barrier properties of ALD oxides are further enhanced by ozone-
101 nucleation (O_3) of the SnO_2 by exposing the C_{60} layer to ozone through an ultrathin (~5 nm)
102 non-conformally grown SnO_2 which functionalizes C_{60} to better nucleate subsequent ALD
103 growth and enable more robust internal barriers in PSCs that can prevent chemical reactions
104 and block the motion of ions, water vapor, and solvents.(20) The deposition of the ozone-
105 nucleated barrier layers does not induce any new degradation modes observed under light and
106 heat testing with T_{90} lifetimes of 500 h and 575 h for PSCs with SnO_2 and $\text{O}_3\text{-SnO}_2$ layers,
107 respectively, at 65°C under approximately 1-sun illumination and quasi-maximum power point
108 (quasi-MPP) set by a static load resistor (ISOS-L2-2I).(20) Furthermore, this O_3 nucleation
109 approach was also shown to reduce the water-vapor transmission rate through the barrier layer
110 and reduce gas, solvent, and halide migration, in turn enhancing PSC stability compared to
111 control devices(20) as well as the mechanical robustness of PSCs compared to SnO_2 .(21)

112 Previous work demonstrated that ion migration in PSCs can be quantified in terms of
113 N_o , which is defined as the number of mobile ions present in the MHP, whereby a significant
114 variation in N_o (5 orders of magnitude) was observed across different samples depending on

115 the composition and chemistry of the top electrode.(22) The reasons for the variation were not
116 well understood at the time. Here, we leverage additional characterization such as Rutherford
117 Backscattering Spectrometry (RBS), a powerful, fast, and non-destructive technique for
118 quantifying elemental motion throughout a PSC. Previous work employed RBS to quantify the
119 depth profile of Pb and I in a film stack comprising $\text{TiO}_2/\text{MAPbI}_3$.(23) More recently, RBS has
120 been utilized to study the radiation hardness and elemental migration, where the RBS results
121 clearly showed the signs of elemental migration of species such as iodine diffusing from the
122 perovskite to the top electrode.(24) In this work, RBS is used to demonstrate that the migration
123 of Ag ions (and of iodine out of the MHP) can be largely mitigated with a thin ALD SnO_2
124 barrier layer between the C_{60} layer and the top Ag electrode. This work also elaborates on
125 several other considerations and implications of N_o that connect to material and device stability,
126 including PSC thermal stability and bulk structural stability.

127

128 **Results and Discussion**

129 **Impact of top electrode chemistry on ion migration**

130 We begin by testing our hypothesis that metal electrodes are contributing/impacting N_o
131 in PSCs with p-i-n architectures by the diffusion of metal ions into the active layer over time
132 or under the influence of environmental stressors such as heat, and that this diffusion can be
133 blocked by barrier layers. N_o measurements of PSCs with and without barrier layers between
134 the device stack and the top electrode were performed using a transient dark current
135 measurement.(22) The control PSC device stack was glass-ITO/ $\text{NiO}_x/\text{Cs}_{0.2}\text{FA}_{0.8}\text{PbI}_3/\text{C}_{60}/(\text{Ag}$
136 or Au or C), as shown in **Fig. 1a**. A SnO_2 layer was introduced for the SnO_2 PSC and $\text{O}_3\text{-SnO}_2$
137 PSC between the C_{60} ETL and the top electrode (Ag or Au or C) (**Fig. 1b and 1c**) deposited on
138 the same substrate to reduce potential variability from different MHP
139 morphologies/microstructures.

140 Starting with the Ag electrode case, from the square data points in **Fig. 1d**, the N_o of
141 the Ag-control PSC was $3.0 * 10^{14} \text{ cm}^{-3}$. The introduction of barrier layers results in a decreased
142 N_o value of $1.0 * 10^{13} \text{ cm}^{-3}$ for the Ag- SnO_2 PSC and $1.2 * 10^{13} \text{ cm}^{-3}$ for the Ag- $\text{O}_3\text{-SnO}_2$ PSC.
143 We hypothesize that the more than 10x increase in N_o for the control PSC is due to the diffusion
144 of mobile Ag ions into the MHP lattice through the C_{60} layer. By contrast, when the denser
145 SnO_2 barrier layers (both SnO_2 and O_3 nucleated SnO_2) were used in the device stack, the
146 diffusion of Ag ions was more effectively blocked. This phenomenon has been validated using
147 other characterization methods where diffusion barriers were employed in the device stack to
148 prevent the diffusion and corrosion of the top electrode.(25–27) In this work, the reduction in
149 ion migration is evident by the reduction of N_o values to a magnitude similar to that of the N_o
150 values of the considerably more inert Au top electrode both in the case of SnO_2 PSC and $\text{O}_3\text{-SnO}_2$
151 PSC. As such, all 3 device configurations exhibited similar N_o values for the Au electrode
152 of $\sim 1.7 * 10^{13} \text{ cm}^{-3}$, whereas the control PSC with C top electrode had a N_o of $6.7 * 10^{11} \text{ cm}^{-3}$
153 and both the device configurations with barrier layers and C top electrode had a N_o of $3 * 10^{12}$
154 cm^{-3} . The slightly reduced value of N_o in the control PSC when compared to the SnO_2 PSC and
155 $\text{O}_3\text{-SnO}_2$ PSC with the C electrode is potentially explained due to two factors. The first is the
156 inertness and chemical stability of C electrodes. The second is the possibility of the C electrode
157 improving the MHP/ C_{60} interface through mechanical toughening an effect that we have

158 previously demonstrated from interfacial fracture energy measurements(28) which results in a
159 more physically dense barrier that possibly suppresses the formation of halide vacancies.(29)

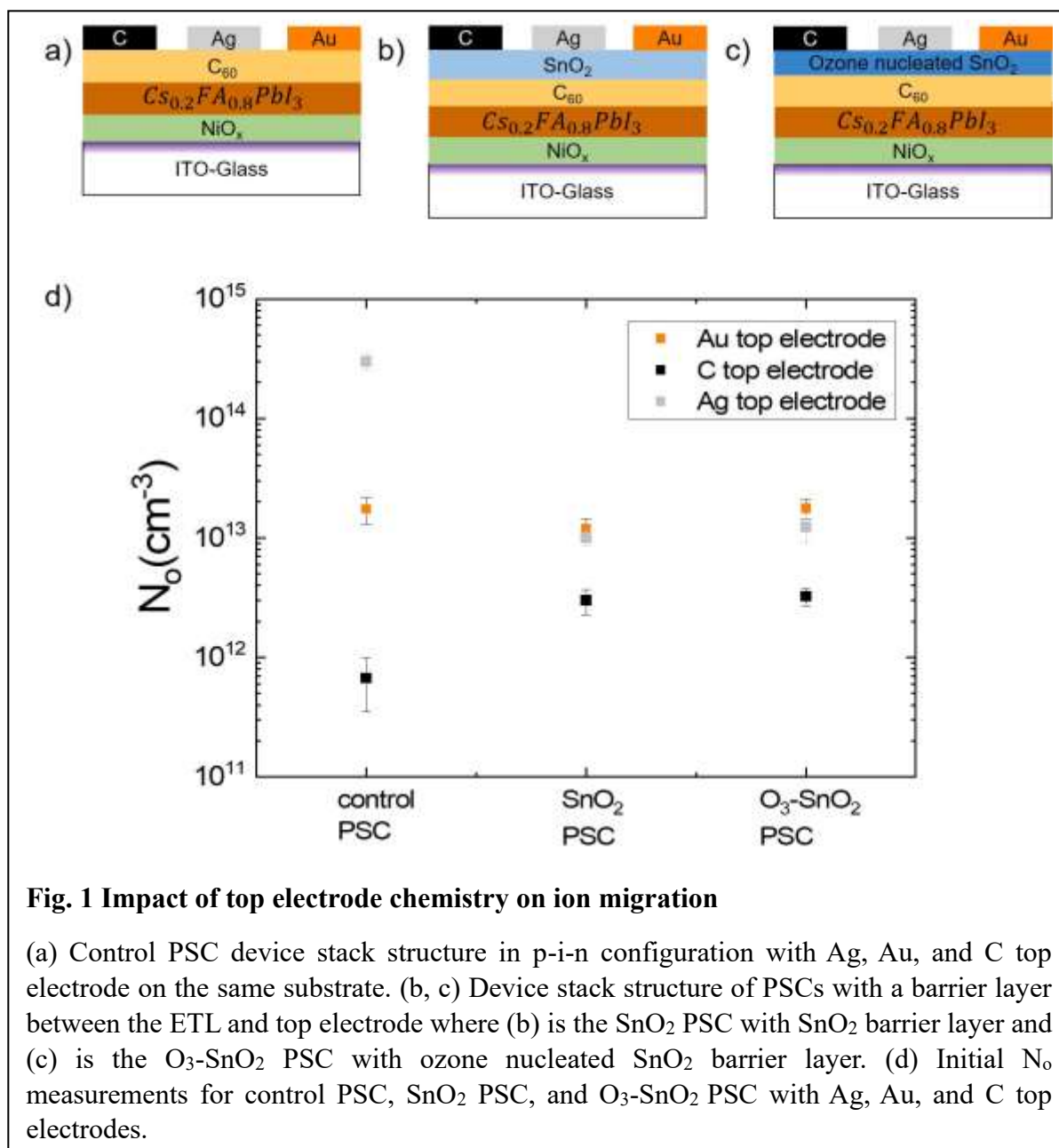


Fig. 1 Impact of top electrode chemistry on ion migration

(a) Control PSC device stack structure in p-i-n configuration with Ag, Au, and C top electrode on the same substrate. (b, c) Device stack structure of PSCs with a barrier layer between the ETL and top electrode where (b) is the SnO_2 PSC with SnO_2 barrier layer and (c) is the $\text{O}_3\text{-SnO}_2$ PSC with ozone nucleated SnO_2 barrier layer. (d) Initial N_o measurements for control PSC, SnO_2 PSC, and $\text{O}_3\text{-SnO}_2$ PSC with Ag, Au, and C top electrodes.

160 Effectiveness of SnO_2 barrier layer in the prevention of Ag ion diffusion

161 In addition to the initial N_o , we measured ion evolution under elevated temperatures to
162 study the extent to which additional ion diffusion occurs in the MHP layer. Aging was
163 performed on the PSCs by subjecting them to 50°C for a period of 120 h. The percentage change
164 in N_o for all 3 PSC device configurations with respect to the 3 top electrodes was observed
165 after aging (Fig. S1-S3). The Ag- SnO_2 and Ag- $\text{O}_3\text{-SnO}_2$ PSCs had an increase of approximately
166 740 \pm 335% and 90 \pm 46% in N_o , respectively, while the N_o of the Ag-control PSC decreased
167 by 35 \pm 9% (Fig. 2a). The N_o value is believed to be a result of the combination of opposing
168 effects from Ag species reacting with the MHP to generate additional mobile ions and halide
169 ions escaping the MHP lattice to reduce mobile ions after mild thermal aging. This can be seen

170 by the reduction of N_o measured after thermal aging in the control sample without a SnO_2
171 barrier layer an effect we attribute to halide ions escaping the MHP lattice and triggering
172 chemical reactions with adjacent layers along with decomposition of the MHP in the bulk, an
173 effect which is shown in **Fig. 4**. However, we believe that in the case of Ag-SnO_2 and $\text{Ag-O}_3-\text{SnO}_2$
174 PSC where a barrier layer is present, the measured increase in N_o after aging is primarily
175 a result of metal diffusion into the MHP. In absolute terms, the measured N_o for aged Ag-control
176 PSCs was still markedly higher than the N_o of aged Ag-SnO_2 and $\text{Ag-O}_3-\text{SnO}_2$ PSCs. After
177 aging, no significant changes in N_o were observed for PSCs with Au and C top electrodes. A
178 relatively minor decrease ($< 50\% \Delta N_o$) is one that we previously observed in MHPs with C
179 electrodes. We hypothesize that the mechanism for the minor decrease is due to the possible
180 onset of film degradation based on a slight redshift in photoluminescence after aging under
181 these conditions(28), which could correspond with mobile ions escaping the MHP lattice.

182 The above observations strongly indicate that mobile Ag species and MHP-Ag
183 reactions are responsible for the changes in N_o . To probe the redistribution of elements in the
184 devices and confirm the observations, RBS was performed on Ag devices for unaged samples
185 and for thermally aged samples that were subjected to the same thermal aging (50 °C for 120
186 h) (**Fig. S4 – S6 and Table S1 - S6**). Subsequently, the atomic concentration of elements in all
187 the layers of the device stack was used to understand the roles of Ag and barrier layers affecting
188 ion diffusion in PSCs. **Fig. 2b** depicts the atomic concentration of Ag in the MHP layer and
189 other PSC layers (C_{60} layer for Ag-control PSC, C_{60} and SnO_2 layer for Ag-SnO_2 PSC, and C_{60}
190 and O_3-SnO_2 layer for $\text{Ag-O}_3-\text{SnO}_2$ PSC) between the MHP and the top electrode for both
191 unaged and aged samples. Note the unaged and aged sample measurements were not performed
192 on the exact same sample before and after aging, which could lead to minor discrepancies in
193 the absolute numbers between samples. There was no significant change in the atomic
194 concentration of Ag in the ETL layers before and after aging with a maximum increase in the
195 atomic concentration of $\sim 0.5 * 10^{16}$ atoms/cm² (**Fig. 2b**) with the amount of uncertainty as
196 explained in **Supplementary Note 1**. However, a significant increase in the atomic
197 concentration of Ag in the MHP layer was found based on model fitting for all PSCs after aging
198 with almost an eight-fold increase for Ag-control PSC from $1.0 * 10^{16}$ to $7.5 * 10^{16}$ atoms/cm²,
199 approximately a four-fold increase for Ag-SnO_2 PSC from $1.4 * 10^{16}$ to $6.0 * 10^{16}$ atoms/cm²,
200 and approximately a two-fold increase for $\text{Ag-O}_3-\text{SnO}_2$ PSC from $1.2 * 10^{16}$ to $3.0 * 10^{16}$
201 atoms/cm². Additionally, even though the atomic concentration of Ag increased in the Ag-
202 control PSC after aging, the atomic concentration of iodine is simultaneously reduced (**Fig. S7**)
203 in the MHP layer. As previously discussed, these opposing effects on N_o likely lead to the
204 overall reduction in N_o observed in **Fig. 2a**. The increase in the atomic concentration of Ag in
205 the MHP layer for all 3 device configurations after aging confirms that the MHP is reacting
206 with Ag without a SnO_2 barrier layer, and Ag ions are diffusing into the MHP layer over time.
207 It is also clear that O_3-SnO_2 PSC is most effective in reducing the diffusion of Ag into the MHP.
208 The RBS data also shows that no iodine is evident in the layers above the MHP after aging in
209 either the SnO_2 or O_3-SnO_2 device configurations (**Table S4 and S6**), a further indication of

210 the mechanism for N_o increase in both of those cases being in part due to Ag diffusion into the
211 MHP and doping the material.

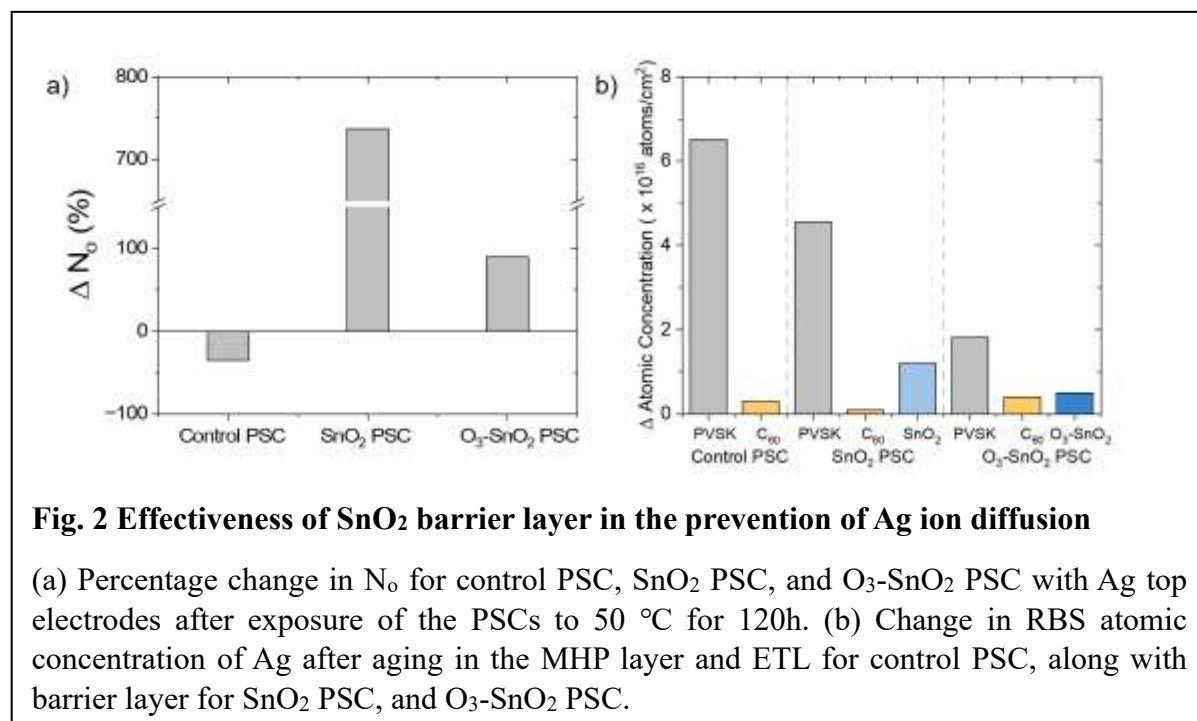


Fig. 2 Effectiveness of SnO_2 barrier layer in the prevention of Ag ion diffusion

(a) Percentage change in N_o for control PSC, SnO_2 PSC, and $\text{O}_3\text{-SnO}_2$ PSC with Ag top electrodes after exposure of the PSCs to 50 °C for 120h. (b) Change in RBS atomic concentration of Ag after aging in the MHP layer and ETL for control PSC, along with barrier layer for SnO_2 PSC, and $\text{O}_3\text{-SnO}_2$ PSC.

212 Threshold in N_o for operation and improved thermal stability of PSCs with barrier layer

213 Accelerated thermal stability tests in the form of *in-situ* N_o -temperature measurements
214 were performed for Ag devices, to evaluate the correlation between ion migration and thermal
215 stability. The *in-situ* N_o measurements were undertaken from 300 K to 450 K with a
216 temperature ramp rate of 10K/min, a tolerance of 0.5K, and a settling time of 20s. We note that
217 thermal tests in the dark were selected to directly probe metal diffusion rather than other forms
218 of instability that arise with heat + light.

219 The point at which no electronic or ionic response was observed in the device was
220 determined and this threshold temperature was assessed for the different architectures. We note
221 that the apparent threshold temperatures may be either kinetic or thermodynamic effects
222 associated with this temperature ramp experiment. The details of the kinetics of the migration
223 are beyond the current scope of this work. Here, the HTL was either a self-assembled
224 monolayer (SAM) (SAM-based PSC with the control architecture) or NiOx layer (control,
225 SnO_2 , and $\text{O}_3\text{-SnO}_2$ PSCs) (**Fig. 3a and 3b**). A SAM-based PSC was selected as all state-of-
226 the-art device architectures utilize SAM as the HTL and to demonstrate the versatility of the
227 technique in measuring different device stack structures. From **Fig. 3c**, the SAM-based PSC
228 and control PSC showed a threshold temperature of 370 K (~100 °C), and the PSCs with barrier
229 layers continued to operate with some response at a temperature of 450 K (~180 °C), the upper
230 limit which was tested for this study. **Fig. S8** shows device failure for the control PSC with a
231 loss in dark IV response beyond 370 K and the SAM-based PSC showing a deteriorated dark
232 IV response at 370K. In comparison, the SnO_2 PSC showed an acceptable dark IV response at
233 450 K while the $\text{O}_3\text{-SnO}_2$ PSC showed an onset of degradation at 440 K, but both the PSCs
234 still had measurable N_o values at 450 K. It is still expected that this is close to the threshold
235 temperature for their ionic response based on the worsening of the IV curves. This effect was

236 validated by testing a second set of samples with a similar top contact configuration in **Fig. S9**
 237 and **S10**, in which case the O_3 -SnO₂ PSCs had an improved thermal stability response
 238 compared to both the control and SnO₂ PSCs. In this case, N_0 values for the control were
 239 measurable up to 450K, although the J-V response exhibited similar degradation at 370K and
 240 above. We note that a BCP layer was also included in this batch, and additional N_0
 241 measurements for control devices that contain the BCP aged at 50°C are included in **Fig. S11**,
 242 where the PSCs with BCP exhibited a trend in N_0 that is very similar to control PSCs without
 243 BCP. This indicates that the introduction of barrier layers in the device stack increased the
 244 threshold operating temperature of the PSCs by at least 80 °C, allowing an unencapsulated PSC
 245 in this work to function with an Ag electrode at a temperature comparable to the state-of-the-
 246 art achieved by a metal-free top contact structure using a combination of ITO with an ALD-
 247 based nanolaminate on top of the PSC for additional extrinsic stability shown elsewhere.(30)

248 Interestingly, there appears to be an empirically observed upper threshold of N_0 for operation
 249 at $\sim 3.0 \times 10^{16} \text{ cm}^{-3}$ for multiple different combinations of electron and hole-transporting layers
 250 with Ag contacts, as indicated by the purple dashed line in **Fig. 3c** above which there is a high
 251 possibility of device failure based on the worsening or complete loss of dark IV response for
 252 most of the samples as shown in **Fig. S8**. All the PSCs showed an increase in N_0 with
 253 temperature throughout the temperature range that was tested but the PSCs that had lower N_0
 254 initially (SnO₂ PSC and O_3 -SnO₂ PSC) were operational at higher temperatures (370K to 450K)
 255 when compared to the PSCs that had higher N_0 initially (control PSC and SAM-based PSC)

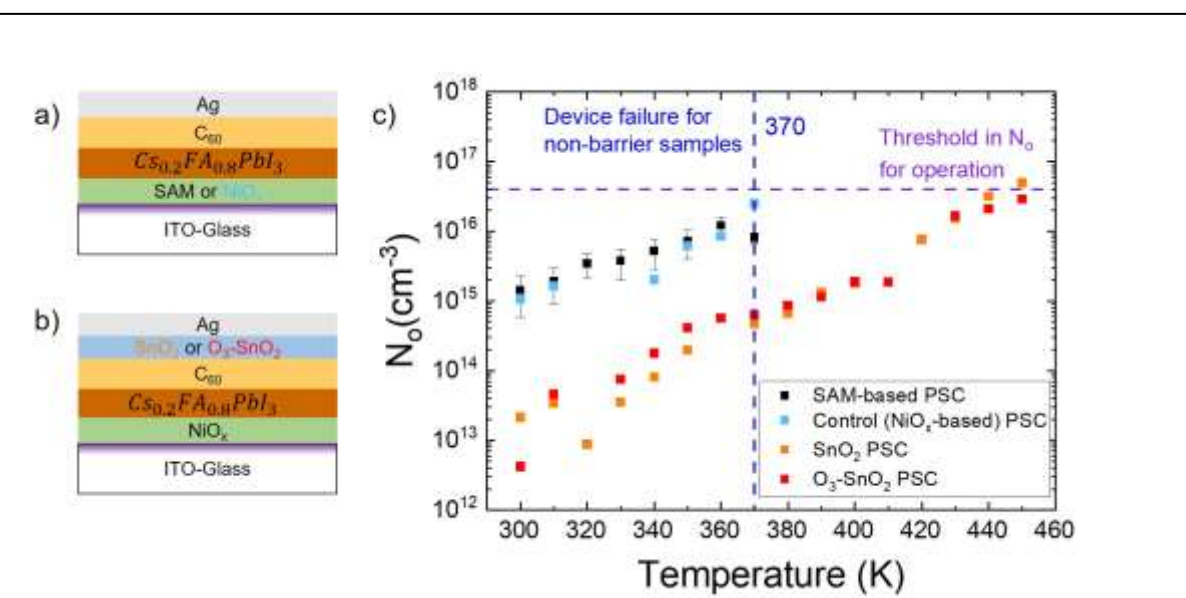


Fig. 3 Threshold in N_0 for operation and improved thermal stability of PSCs with barrier layer

(a) Device stack structure in p-i-n configuration for control and SAM-based PSC with an HTL of NiO_x and SAM respectively. (b) Device stack structure in p-i-n configuration for SnO₂ PSC and O_3 -SnO₂ PSC with a barrier layer of SnO₂ and O_3 -SnO₂ respectively between ETL and the top electrode. (c) N_0 of PSCs versus temperature, showing threshold operating points of the devices at higher temperatures and also the threshold in N_0 for operation.

which failed to show a response beyond 370K. There are multiple interpretations of this observation, all of which are in line with higher N_o values corresponding to accelerated degradation. One possible mechanism for this observation could be due to other failure modes unrelated to metal diffusion, such as reactions at the HTL/perovskite interface. This shows that having a higher N_o initially is consistent with more rapid deterioration of PSCs at higher temperatures and that having a lower initial N_o appears to be one of the factors that are associated with improved thermal stability of these p-i-n PSCs. As such, there is the possibility of implementing N_o as a screening tool or quality control for validating barrier layer efficacy in PSCs after fabrication.

Improved bulk MHP stability of PSCs with barrier layer

To study how the changes in ions correlate to microstructure changes in the films, GIWAXS was performed on control, SnO_2 , and $\text{O}_3\text{-SnO}_2$ PSCs before and after the PSCs were subjected to the same thermal aging (50°C for 120h in N_2). Incident angle scans showcasing the X-ray diffraction plots in q-space at incidence angles 0.3° (representing the top surface) and 5° (representing the bulk) for all 3 device configurations before and after aging are shown in **Fig. 4**. Note that the unaged and aged sample measurements were not performed on the same sample. The peaks that indicate some presence of the degradation products were evident on the MHP surface for all the PSCs before and after aging was performed. All the unaged PSCs (**Fig. 4a-c**) showcased a clear MHP (110) peak in the bulk.(31) However, after aging, the control PSC (**Fig. 4d**) exhibited a significant diminishing of the MHP (110) peak in the bulk. Note that a slightly higher amount of degradation was observed on the surface in the SnO_2 PSC (**Fig. 4e**) when compared to the $\text{O}_3\text{-SnO}_2$ PSC (**Fig. 4f**) after aging. Both SnO_2 PSC and $\text{O}_3\text{-SnO}_2$ PSC did not show a significant variation in the bulk 1D profile after aging i.e., they retained their MHP (110) peak along with no presence of degradation byproduct peaks. The integrated peak area ratios of MHP (110) and a degradation product (which we hypothesize corresponds to either 2H- FAPbI_3 or a non-perovskite phase) (**Table S7**) from the 1D integrated GIWAXS profiles show that this ratio reduced from unaged to aged samples in the decreasing order of control PSC, SnO_2 PSC, and $\text{O}_3\text{-SnO}_2$ PSC. This reduction indicates that the control PSC has low stability both in the top surface and the bulk, whereas SnO_2 PSCs and $\text{O}_3\text{-SnO}_2$ PSCs show an improvement in bulk stability after the introduction of the barrier layers in the device structure.

In addition to the dark I-V measurements, a full set of measurements were performed in the light and complemented by temperature-dependent EQE for the $\text{O}_3\text{-SnO}_2$ PSC (showing a minor increase in bandgap with temperature as in line with previous reporting for PSCs with similar compositions(32)) as shown in **Fig. S12 and S13**. Control PSCs exhibited a rapid performance degradation with an increase in temperature, whereas $\text{O}_3\text{-SnO}_2$ PSCs exhibited much better thermal stability. There was a continuous drop in power conversion efficiency (PCE) from 14.5% to 6.6% for control PSC, whereas the PCE dropped from 16% to 12% for $\text{O}_3\text{-SnO}_2$ PSCs when the devices were exposed to heat from 300K to 450K. The factors contributing to the drop in PCE of control PSCs are a drop in V_{oc} and fill factor, both of which showed better stability for $\text{O}_3\text{-SnO}_2$ PSCs. Hence the improvement in N_o and the associated enhancement in the $\text{O}_3\text{-SnO}_2$ PSCs in comparison to control PSCs is complemented by better stability under extreme operational conditions (**Fig. S14**) and is on par with the best reported thermal stability of PSCs, which required the use of a metal-free top contact structure comprising ITO and an ALD nanolaminate(30) on top of the completed device. Our device

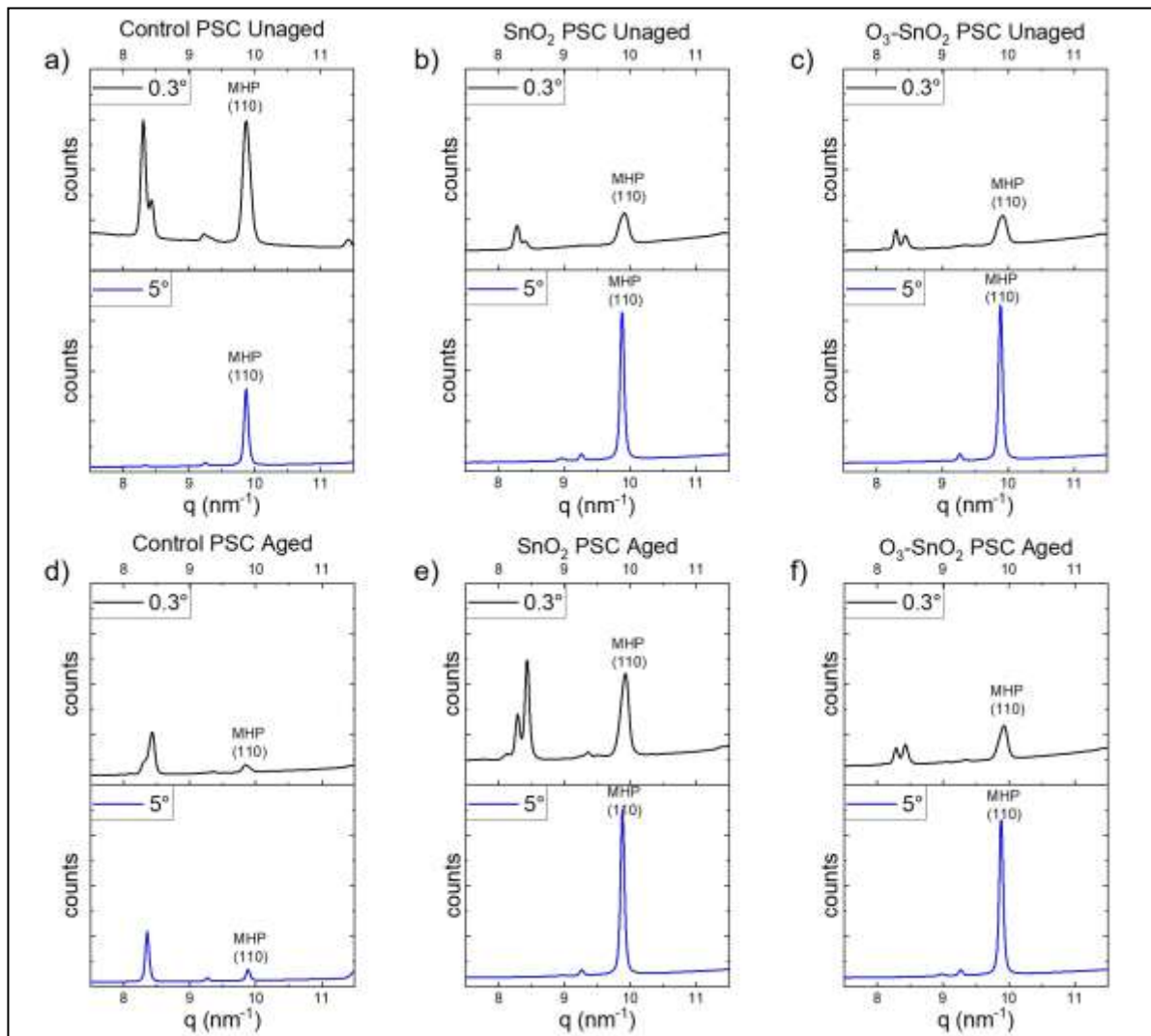


Fig. 4 Improved bulk MHP stability of PSCs with barrier layer

X-ray diffraction plots in q-space at incidence angles 0.3° (representing the top surface) and 5° (representing the bulk) (a, b, c) unaged PSCs, and (d, e, f) PSCs subjected to $50\text{ }^\circ\text{C}$ for 120h. (a, d) control PSC, (b, e) SnO_2 PSC, and (c, f) $\text{O}_3\text{-SnO}_2$ PSC.

301 structure shows that the reactions from a highly reactive metal (Ag) can be mitigated by
 302 preventing ion diffusion through the use of an ultra-thin, dense, and well-designed built-in
 303 barrier layer.

304 The activation energy (E_A) of the PSCs was also determined using *in-situ* ionic
 305 conductivity across a range of temperatures, a measurement that has been used in several other
 306 reports for ion-specific activation mechanisms.(33–35) As plotted in **Fig. S15 and S16**, the E_A
 307 of the control PSC was **0.346** eV, the E_A of the SAM-based PSC was **0.410** eV, and the E_A of
 308 the $\text{O}_3\text{-SnO}_2$ PSC was **0.503** eV. This value is much higher than the E_A of triple halide PSCs
 309 with a similar architecture to the control PSC in this study and without any barrier layer (0.14
 310 eV) from previous work.(22) As expected, these values support that the mobile ion activation
 311 is suppressed in the PSCs with a barrier layer when compared to the control and SAM-based
 312 PSCs. The implication of a higher E_A in the $\text{O}_3\text{-SnO}_2$ PSC demonstrates that well-designed

313 barrier layers can reduce both the formation and evolution of mobile ions under operational
314 conditions.

315 The primary focus of this work was utilizing the ion blocking feature/mechanism of a
316 dense ALD O_3 - SnO_2 layer to clearly show the diffusion of metal into the MHP under operation
317 and the ability to detect this diffusion using N_o . A mild temperature of 50°C was initially
318 selected for the exposure tests to be able to observe only the temperature-dependent diffusion
319 mechanisms on the PSCs without the influence of more rapid MHP degradation that could
320 happen if the accelerated testing was done at higher temperatures or with light. Once an
321 understanding regarding the diffusion of metal was achieved at 50°C, the PSCs were exposed
322 to much higher temperatures up to 450K (177°C) to observe the effects of degradation of MHP
323 along with the diffusion of metal into the MHP. Additional experiments were performed under
324 illumination during this high-temperature study showing the improved operational stability of
325 O_3 - SnO_2 devices compared to control devices (**Fig. S12 and S13**) that directly correlate with
326 the reduction in N_o . Future work will include in-situ PL mapping characterization of the PSCs
327 to monitor compositional changes in the MHP caused by the metal diffusion under operation
328 during thermal aging.

329 Conclusion

330 In this work, we quantified mobile ionic species directly or indirectly resulting from
331 chemical reactions. We demonstrated that our N_o measurement is sensitive to Ag ions diffusing
332 into the MHP lattice of PSCs through the changes in N_o based on top electrode chemistry and
333 from thermal aging. We validated that O_3 - SnO_2 is an improved barrier layer in preventing the
334 diffusion of Ag ions along with retaining the bulk stability of the MHP while improving PSC
335 thermal stability compared to devices without a barrier layer. This allowed us to correlate this
336 N_o metric to current-voltage (IV) behavior and ion redistribution as measured by Rutherford
337 Backscattering Spectrometry. It is important to note that at high enough temperatures such as
338 450K, MHPs will degrade even with barrier layers due to structural degradation, an effect
339 which was observed in the appearance of an upper threshold for N_o across device types. While
340 many factors contribute to the real lifetime of fielded PV modules, the effectiveness, and
341 reproducibility of barrier layers to prevent ion migration and chemical degradation are among
342 the most critical to tackle for the stability of PSCs. Overall, our results demonstrate that N_o -
343 temperature measurements are a rapid and effective method to characterize barrier layers at
344 perovskite/electrode interfaces and predict the chemical robustness of the full devices.

345 To this end, there is a need for a deeper understanding of the correlation between power
346 conversion efficiency, ion migration, and stability of PSCs. As such, we believe that the use of
347 N_o measurements coupled with accelerated thermal and/or light aging can serve as a highly
348 useful tool in quantifying the extent to which multiple sources of ions (whether from the top
349 electrode or from the MHP itself) move throughout the PSC to provide a deeper understanding
350 of ion-based degradation mechanisms.

351 Methods

352 The preparation of glass substrates before doing any of the processing on top of the
353 substrate was performed in a step-by-step procedure as follows: Indium tin oxide coated glass
354 (ITO-glass) substrates (Xin Yan Technologies) were initially cleaned in an ultrasonic cleaner
355 by submerging them in an industry grade soap solution of Extran (Millipore Sigma) diluted in

356 water in the ratio of 1:10 for 10 min. Then, the ITO-glass slides were rinsed under a flow of
357 de-ionized water with a brush to remove the residual soap on top of the substrates. This was
358 followed by ultrasonic cleaning by submerging them in isopropyl alcohol (IPA) (Thermo
359 Scientific) and acetone (Alfa Aesar – 99.5%+) separately for 10 min. Finally, they were
360 subjected to a UV ozone treatment for another 15 min.

361 *Nickel-oxide (NiO_x)*

362 A NiO_x sol-gel solution for depositing the hole transport layer (HTL) was prepared by
363 mixing 1M NiNO₃·(H₂O)₆ (Sigma Aldrich – 99.999% trace metals basis) in 94% ethylene
364 glycol (EG) (Thermo scientific – anhydrous 99.8%) and 6% ethylenediamine (EDA) (Thermo
365 scientific – 99%); the vial was then placed in a vortex mixer, and the solution was mixed until
366 it turned a dark blue color.

367 *Self-assembled monolayer*

368 0.5 mg ml⁻¹ MeO-2PACz self-assembled monolayer solution dissolved in ethanol was spin-
369 coated on substrates at 3,000 rpm for 30 s in a nitrogen glovebox, followed by annealing at 100
370 °C for 10 min.

371 *Cesium Formamidinium Lead Iodide (Cs_{0.2}FA_{0.8}PbI₃)*

372 The MHP precursor solution for Cs_{0.2}FA_{0.8}PbI₃ films was prepared by mixing 0.2 mol
373 Cesium Iodide (CsI) (Sigma-Aldrich – 99.999% trace metals basis), 0.8 mol Formamidinium
374 Iodide (FAI) (Greatcell Solar Materials), and 1 mol Lead Iodide (PbI₂) (TCI America – 99.99%
375 trace metals basis). A 1M concentration solution was made by mixing 0.0519 gm of CsI, 0.1375
376 gm of FAI, and 0.461 gm of PbI₂ in a solvent of 4:1 Dimethylformamide (DMF) (Sigma-
377 Aldrich – Anhydrous 99.8%) and Dimethyl Sulfoxide (DMSO) (Sigma-Aldrich – Anhydrous
378 ≥ 99.9%) with 800 μL of DMF and 200 μL of DMSO. A vortex mixer was used to mix the
379 solution until the powders were uniformly dissolved and a yellow solution was formed.

380 *Perovskite Solar Cells (PSCs)*

381 After finishing the substrate preparation process and making the required inks, PSCs
382 were fabricated in a step-by-step process. As the PSCs were in a p-i-n configuration, the HTL
383 (NiO_x/SAM) was first deposited on the cleaned ITO-glass by spin coating. 50μL of NiO_x
384 solution was deposited at a speed of 5000 rpm and an acceleration of 2500 rpm/s for 30 s in a
385 fume hood and then annealed at 315°C for 1h. The SAM layer was deposited at a speed of 3000
386 rpm for 30 s followed by annealing at 100°C for 10 min. After the HTL was formed, the MHP
387 absorber layer of Cs_{0.2}FA_{0.8}PbI₃ was deposited using a spin coating process with anti-solvent
388 quenching. This was done by depositing 100μL of MHP precursor on the glass and spinning at
389 a speed of 1000 rpm and acceleration of 500 rpm/s for 10 s, and then the speed was stepped up
390 to 5000 rpm and acceleration of 1500 rpm/s for 10 s. In the last 3-5 s of the second step, 100μL
391 of chlorobenzene (anti-solvent) (Sigma-Aldrich – Anhydrous 99.8%) was deposited quickly.
392 Then, the samples were annealed at 150 °C for 10 minutes. The ETL was deposited by
393 evaporating 45nm of C₆₀ on top of the samples in an Angstrom evaporator with a shadow mask,
394 and the top electrode was made by evaporating either 100 nm of Ag or Au on top of the device
395 stack using a different mask. The carbon (C) top electrode was formed on top of the PSC by
396 depositing it from the solvent-based C paste (PELCO conductive carbon glue – Ted Pella).
397 Three different electrodes (evaporated Ag or Au and a solvent-based C) were deposited on top

398 of the same PSC substrate to observe the variation in N_o with respect to barrier layers and the
399 top electrode. ALD SnO_2 and $\text{O}_3\text{-SnO}_2$ for the barrier layers were deposited in a Beneq TFS200
400 ALD reactor by 125 cycles of tetrakisdimethylamino tin(IV) and water at 90. A 15-second
401 ozone and water treatment was applied to the $\text{O}_3\text{-SnO}_2$ samples *in-situ* part way through the
402 125 cycles SnO_2 deposition following the sequence: 40 cycles SnO_2 /15-second ozone and
403 water/ 85 cycle SnO_2 . (20)

404 *Characterization*

405 All the ionic and electronic measurements were performed with PAIOS, an all-in-one
406 measurement equipment for photovoltaic devices and LEDs (FLUXiM AG). A hot plate was
407 used to age the PSCs (as fabricated without encapsulation) at 50 °C in an N_2 glovebox for 120h
408 with *ex-situ* measurements on PAIOS. N_o was measured and calculated using the transient dark
409 current method (**Fig. S17**) as described in our previous work(22) in which a voltage bias of 800
410 mV is applied to the PSC in a forward-bias configuration in the form of a pulse with the
411 following characteristics: 1 ms settling time, 10 ms pulse time, and 1 ms follow-up time. The
412 entire measurement lasts around 13 ms with the measurement cut-off around 1 ms after the bias
413 is taken away, during which the mobile ions in the MHP drift. The measured drift current can
414 be time-integrated and divided by the elementary charge, area, and thickness of the MHP layer
415 respectively to determine the N_o .(22) For the quantification of mobile ion concentration (N_o)
416 using the transient dark current methodology, the voltage pulse is applied in forward bias for
417 only a short time of 10ms. This timescale was chosen to be able to only measure the intrinsic
418 concentration of ions in the perovskite that are ready to move under a small voltage
419 perturbation. Using such a short timescale for the measurement might result in values of N_o
420 that are lower than what has been reported in the literature, but we believe that the values
421 obtained represent the actual ionic concentration present in the device at the surface level or at
422 the interfaces. The consistency of the measured N_o values has been shown in our previous
423 works.(22,28,35)

424 *In-situ* ionic measurements were performed with the temperature control stage and
425 module (LTS-420E) from Linkam in integration with PAIOS in increments of 10 K from room
426 temperature (300 K) up to 450 K. E_A was measured following the same methodology used in
427 our previous work.(35) The ramp rate used was 10K/min and the tolerance was 0.5K with a
428 settling time of 20s. The reported E_A values are based on measurements of a single sample.
429 However, the samples were measured during both ramp up and ramp down of the temperature.
430 The reduction of temperature happened naturally and hence the samples would have significant
431 dwell at each temperature and the calculations include averages of the measurement in both
432 directions.

433 The RBS experiment was conducted in the Ion beam laboratory (IBL) at the University
434 of North Texas (UNT) using the NEC 9SH 3MV Pelletron accelerator.(36,37) All the
435 experiments were performed in the ion microprobe beamline using a 2 MeV He^+ beam under
436 a vacuum of 2×10^{-7} Torr. The RBS spectra were collected using a Passivated Implanted Planar
437 Silicon (PIPS) charged particle detector from Mirion Technologies (Canberra), model No.
438 PD25-11-300 AM, having a solid angle of 34 milli-steradian, and the operating voltage for the
439 detector was 40 V situated at the backscattered angle of 145° (**Fig. S18**). The detector
440 arrangement in the microprobe chamber is such that the incident beam, backscattering detector,
441 and target normal lie in the same horizontal plane.

442 The RBS data fitting was done using the SIMNRA software package.(38) Based on the
443 thickness values of each layer in the PSC stack, a simulated sample was generated. The
444 concentrations of each layer were adjusted until a suitable match was achieved. Layer thickness
445 is accepted by SIMNRA in the form of the layer's areal density (atoms cm⁻²). The SRIM/TRIM
446 software program was utilized to convert the thickness into areal density(39) and detailed
447 information on the process is provided elsewhere.(24) The layer information extracted from
448 the SIMNRA was fed into the MultiSIMNRA(40) software program, to further extract the
449 contribution from the individual layers and their elemental species.

450 To identify the different crystalline phases in the perovskite films and devices, at
451 different subsurface depths, synchrotron-based grazing incidence wide-angle X-ray scattering
452 (GIWAXS) data were collected at NCD-SWEET beamline at the ALBA synchrotron
453 (Cerdanyola del Vallès, Spain): a monochromatic ($\lambda=0.95741$ Å) X-ray beam of $150 \times 30 \mu\text{m}^2$
454 [H × V] was defined using a Si (111) channel cut monochromator and collimated using Be
455 Compound Refractive Lenses (CRLs). The scattered signal was recorded using a Rayonix
456 LX255-HS area detector placed at 251.2 mm from the sample position. Detector tilts and
457 sample-to-detector distance were calculated using Cr₂O₃ as a calibrant, which was employed
458 to calibrate the reciprocal space wavevector, q . GIWAXS frames were recorded at incident
459 angles (α_i) between 0° and 5° in a scanning fashion, shifting from the surface-sensitive
460 evanescent regime of scattering and transitioning to a deep penetrative measurement of the film
461 layers at relatively high angles.(41) Throughout the data acquisition process, a continuous flow
462 of N₂ gas was maintained over the sample. Collected 2D images were azimuthally integrated
463 to general 1D profiles using PyFAI(42) and processed using a custom Python routine.

464 Acknowledgments

465 This material is based upon work supported by the National Science Foundation under Grant
466 No. 2339233. This work was authored in part by the National Renewable Energy Laboratory,
467 operated by Alliance for Sustainable Energy, LLC, for the U.S. Department of Energy (DOE)
468 under Contract No. DE-AC36-08GO28308. A.P., J.J.B., and R.A.K. acknowledges financial
469 support from the U.S. Department of Energy's Office of Energy Efficiency and Renewable
470 Energy (EERE) under Solar Energy Technologies Office (SETO) Agreement DE-EE0009513.
471 The views expressed in the article do not necessarily represent the views of the DOE or the
472 U.S. Government. J.A.S. acknowledges financial support from the Australian Research Council
473 (ARC: grant no. DE230100173. J.A.S., R.A.S., and M.B.J.R. thank the staff of the BL11 NCD-
474 SWEET beamline for their assistance in recording the synchrotron GIWAXS data. R.A.S. and
475 M.B.J.R. acknowledge financial support from iBOF-21-085 PERsist and Internal Funds KU
476 Leuven (C14/23/090). B.R., M.S., and M.P. acknowledge financial support from the U.S.
477 National Science Foundation Grant No. ECCS-2210722.

478 Author Contributions

479 Conceptualization, S.P. and N.R.; methodology, S.P. and N.R.; investigation, S.P., M.N.K.,
480 M.S., M.P., M.C., R.A.S., and E.S.; validation S.P. and R.A.K.; formal analysis S.P., M.N.K.,
481 M.S., M.P., and J.A.S.; data curation S.P.; visualization S.P. and N.R.; writing – original draft,
482 S.P. and N.R.; writing – review & editing S.P., M.N.K., M.S., M.P., M.A.D., R.A.K., M.C.,
483 R.A.S., E.S., M.B.J.R., I.R.S., V.R.W., J.J.B., J.M.L., J.A.S., A.P., B.R., and N.R.; resources S.P.,
484 M.C., I.R.S., J.M.L., M.A.D., J.A.S., A.P., and B.R.; visualization S.P. and N.R.; software S.P.,
485 M.N.K., M.S., M.P., and J.A.S.; supervision M.B.J.R., I.R.S., V.R.W., J.J.B., J.M.L., J.A.S.,

486 A.P., B.R., and N.R.; project administration N.R.; funding acquisition M.B.J.R., J.J.B., J.M.J.,
487 J.A.S., A.P., B.R., and N.R.; All the authors discussed the results and commented on the
488 manuscript

489 **Conflict of Interest**

490 S.P. and N.R. have filed for a patent based on this work. The other authors declare no conflict
491 of interest.

492 **Data Availability Statement**

493 The data that support the findings of this study are available from the corresponding author
494 upon reasonable request

495 **References**

- 496 1. Li Z, Li B, Wu X, Sheppard SA, Zhang S, Gao D, et al. Organometallic-functionalized
497 interfaces for highly efficient inverted perovskite solar cells. *Science* (1979) [Internet].
498 2022 Apr 22;376(6591):416–20. Available from: <https://doi.org/10.1126/science.abm8566>
- 500 2. Yoo JJ, Seo G, Chua MR, Park TG, Lu Y, Rotermund F, et al. Efficient perovskite solar
501 cells via improved carrier management. *Nature* [Internet]. 2021;590(7847):587–93.
502 Available from: <https://doi.org/10.1038/s41586-021-03285-w>
- 503 3. NREL Best Research-Cell Efficiency Chart [Internet]. [cited 2024 Aug 15]. Available
504 from: <https://www.nrel.gov/pv/cell-efficiency.html>
- 505 4. Green MA, Ho-Baillie A, Snaith HJ. The emergence of perovskite solar cells. *Nat
506 Photonics* [Internet]. 2014;8(7):506–14. Available from: <https://doi.org/10.1038/nphoton.2014.134>
- 508 5. Ashif Mohammad, Farhana Mahjabeen. Promises and Challenges of Perovskite Solar
509 Cells: A Comprehensive Review. *BULLET : Jurnal Multidisiplin Ilmu* [Internet]. 2023
510 Oct 20;2(5):1147–57. Available from: <https://journal.mediapublikasi.id/index.php/bullet/article/view/3685>
- 512 6. Čulík P, Brooks K, Momblona C, Adams M, Kinge S, Maréchal F, et al. Design and Cost
513 Analysis of 100 MW Perovskite Solar Panel Manufacturing Process in Different
514 Locations. *ACS Energy Lett* [Internet]. 2022 Sep 9;7(9):3039–44. Available from:
515 <https://doi.org/10.1021/acsenergylett.2c01728>
- 516 7. Ahangharnejhad RH, Becker W, Jones J, Anctil A, Song Z, Phillips A, et al. Environmental
517 Impact per Energy Yield for Bifacial Perovskite Solar Cells Outperforms
518 Crystalline Silicon Solar Cells. *Cell Rep Phys Sci* [Internet]. 2021;2(2):100344.
519 Available from: <https://www.sciencedirect.com/science/article/pii/S2666386421000291>
- 520 8. Sakhatskyi K, John RA, Guerrero A, Tsarev S, Sabisch S, Das T, et al. Assessing the
521 Drawbacks and Benefits of Ion Migration in Lead Halide Perovskites. *ACS Energy Lett*
522 [Internet]. 2022 Oct 14;7(10):3401–14. Available from: <https://doi.org/10.1021/acsenergylett.2c01663>
- 524 9. Liu J, Hu M, Dai Z, Que W, Padture NP, Zhou Y. Correlations between Electrochemical
525 Ion Migration and Anomalous Device Behaviors in Perovskite Solar Cells. *ACS Energy
526 Lett* [Internet]. 2021 Mar 12;6(3):1003–14. Available from: <https://doi.org/10.1021/acsenergylett.0c02662>

528 10. Grancini G, Roldán-Carmona C, Zimmermann I, Mosconi E, Lee X, Martineau D, et al.
529 One-Year stable perovskite solar cells by 2D/3D interface engineering. *Nat Commun*
530 [Internet]. 2017;8(1):15684. Available from: <https://doi.org/10.1038/ncomms15684>

531 11. Perovskite PV Accelerator for Commercializing Technologies. [cited 2024 Aug 15];
532 Available from: <https://pvpact.sandia.gov/>

533 12. Bi E, Song Z, Li C, Wu Z, Yan Y. Mitigating ion migration in perovskite solar cells.
534 *Trends Chem* [Internet]. 2021 Jul 1;3(7):575–88. Available from:
535 <https://doi.org/10.1016/j.trechm.2021.04.004>

536 13. Zai H, Ma Y, Chen Q, Zhou H. Ion migration in halide perovskite solar cells:
537 Mechanism, characterization, impact and suppression. *Journal of Energy Chemistry*
538 [Internet]. 2021;63:528–49. Available from:
539 <https://www.sciencedirect.com/science/article/pii/S2095495621004290>

540 14. Zhao Y, Zhou W, Han Z, Yu D, Zhao Q. Effects of ion migration and improvement
541 strategies for the operational stability of perovskite solar cells. *Physical Chemistry*
542 *Chemical Physics* [Internet]. 2021;23(1):94–106. Available from:
543 <http://dx.doi.org/10.1039/D0CP04418K>

544 15. Zhao L, Kerner RA, Xiao Z, Lin YL, Lee KM, Schwartz J, et al. Redox Chemistry
545 Dominates the Degradation and Decomposition of Metal Halide Perovskite
546 Optoelectronic Devices. *ACS Energy Lett* [Internet]. 2016 Sep 9;1(3):595–602.
547 Available from: <https://doi.org/10.1021/acsenergylett.6b00320>

548 16. Kerner RA, Zhao L, Harvey SP, Berry JJ, Schwartz J, Rand BP. Low Threshold Voltages
549 Electrochemically Drive Gold Migration in Halide Perovskite Devices. *ACS Energy*
550 *Lett* [Internet]. 2020 Nov 13;5(11):3352–6. Available from:
551 <https://doi.org/10.1021/acsenergylett.0c01805>

552 17. Kerner RA, Cohen A V, Xu Z, Kirmani AR, Park SY, Harvey SP, et al. Electrochemical
553 Doping of Halide Perovskites by Noble Metal Interstitial Cations. *Advanced Materials*
554 [Internet]. 2023 Jul 1;35(29):2302206. Available from:
555 <https://doi.org/10.1002/adma.202302206>

556 18. Shlenskaya NN, Belich NA, Grätzel M, Goodilin EA, Tarasov AB. Light-induced
557 reactivity of gold and hybrid perovskite as a new possible degradation mechanism in
558 perovskite solar cells. *J Mater Chem A Mater* [Internet]. 2018;6(4):1780–6. Available
559 from: <http://dx.doi.org/10.1039/C7TA10217H>

560 19. Zhou J, Liu Z, Yu P, Tong G, Chen R, Ono LK, et al. Modulation of perovskite
561 degradation with multiple-barrier for light-heat stable perovskite solar cells. *Nat*
562 *Commun* [Internet]. 2023;14(1):6120. Available from: <https://doi.org/10.1038/s41467-023-41856-9>

563 20. Johnson SA, White KP, Tong J, You S, Magomedov A, Larson BW, et al. Improving the
564 barrier properties of tin oxide in metal halide perovskite solar cells using ozone to
565 enhance nucleation. *Joule* [Internet]. 2023 Dec 20;7(12):2873–93. Available from:
566 <https://doi.org/10.1016/j.joule.2023.10.009>

567 21. Li M, Johnson S, Gil-Escríg L, Sohmer M, Figueroa Morales CA, Kim H, et al.
568 Strategies to improve the mechanical robustness of metal halide perovskite solar cells.
569 *Energy Advances* [Internet]. 2024;3(1):273–80. Available from:
570 <http://dx.doi.org/10.1039/D3YA00377A>

572 22. Penukula S, Estrada Torrejon R, Rolston N. Quantifying and Reducing Ion Migration in
573 Metal Halide Perovskites through Control of Mobile Ions. *Molecules* [Internet].
574 2023;28(13). Available from: <https://www.mdpi.com/1420-3049/28/13/5026>

575 23. Lang F, Juma A, Somsongkul V, Dittrich T, Arunchaiya M. Rutherford Backscattering
576 Spectroscopy of Mass Transport by Transformation of PbI₂ into CH₃NH₃PbI₃ within
577 np-TiO₂. *Hybrid Materials*. 2014 Jan 22;1(1).

578 24. Parashar M, Sharma M, Saini DK, Byers TA, Luther JM, Sellers IR, et al. Probing
579 elemental diffusion and radiation tolerance of perovskite solar cells via non-destructive
580 Rutherford backscattering spectrometry. *APL Energy* [Internet]. 2024 Mar
581 7;2(1):016109. Available from: <https://doi.org/10.1063/5.0193601>

582 25. Park HH, Fermin DJ. Recent Developments in Atomic Layer Deposition of Functional
583 Overlays in Perovskite Solar Cells. *Nanomaterials* [Internet]. 2023;13(24). Available
584 from: <https://www.mdpi.com/2079-4991/13/24/3112>

585 26. Bi E, Chen H, Xie F, Wu Y, Chen W, Su Y, et al. Diffusion engineering of ions and charge
586 carriers for stable efficient perovskite solar cells. *Nat Commun* [Internet].
587 2017;8(1):15330. Available from: <https://doi.org/10.1038/ncomms15330>

588 27. Li N, Shi Z, Fei C, Jiao H, Li M, Gu H, et al. Barrier reinforcement for enhanced
589 perovskite solar cell stability under reverse bias. *Nat Energy* [Internet]. 2024; Available
590 from: <https://doi.org/10.1038/s41560-024-01579-7>

591 28. Penukula S, Tippin F, Li M, Khawaja KA, Yan F, Rolston N. Use of carbon electrodes
592 to reduce mobile ion concentration and improve reliability of metal halide perovskite
593 photovoltaics. *Energy Materials* [Internet]. 2024;4(5). Available from:
594 <https://www.oaepublish.com/articles/energymater.2024.26>

595 29. Zhong Y, Yang J, Wang X, Liu Y, Cai Q, Tan L, et al. Inhibition of Ion Migration for
596 Highly Efficient and Stable Perovskite Solar Cells. *Advanced Materials* [Internet]. 2023
597 Dec 1;35(52):2302552. Available from: <https://doi.org/10.1002/adma.202302552>

598 30. Afshari H, Sourabh S, Chacon SA, Whiteside VR, Penner RC, Rout B, et al. FACsPb
599 Triple Halide Perovskite Solar Cells with Thermal Operation over 200 °C. *ACS Energy*
600 Lett [Internet]. 2023 May 12;8(5):2408–13. Available from:
601 <https://doi.org/10.1021/acsenergylett.3c00551>

602 31. Yang Y, Yang L, Feng S. Interfacial engineering and film-forming mechanism of
603 perovskite films revealed by synchrotron-based GIXRD at SSRF for high-performance
604 solar cells. *Mater Today Adv* [Internet]. 2020;6:100068. Available from:
605 <https://www.sciencedirect.com/science/article/pii/S2590049820300151>

606 32. Moot T, Patel JB, McAndrews G, Wolf EJ, Morales D, Gould IE, et al. Temperature
607 Coefficients of Perovskite Photovoltaics for Energy Yield Calculations. *ACS Energy*
608 Lett [Internet]. 2021 May 14;6(5):2038–47. Available from:
609 <https://doi.org/10.1021/acsenergylett.1c00748>

610 33. López-González MC, del Pozo G, Arredondo B, Delgado S, Martín-Martín D, García-
611 Pardo M, et al. Temperature behaviour of mixed-cation mixed-halide perovskite solar
612 cells. Analysis of recombination mechanisms and ion migration. *Org Electron* [Internet].
613 2023;120:106843. Available from:
614 <https://www.sciencedirect.com/science/article/pii/S156611992300099X>

615 34. Xing J, Wang Q, Dong Q, Yuan Y, Fang Y, Huang J. Ultrafast ion migration in hybrid
616 perovskite polycrystalline thin films under light and suppression in single crystals.

617 Physical Chemistry Chemical Physics [Internet]. 2016;18(44):30484–90. Available
618 from: <http://dx.doi.org/10.1039/C6CP06496E>

619 35. Sun J, Penukula S, Li M, Hosseinzade MR, Tang Y, Dou L, et al. Mechanical and Ionic
620 Characterization for Organic Semiconductor-Incorporated Perovskites for Stable 2D/3D
621 Heterostructure Perovskite Solar Cells. Small [Internet]. 2024 Oct 7;n/a(n/a):2406928.
622 Available from: <https://doi.org/10.1002/smll.202406928>

623 36. Rout B, Dhoubhadel MS, Poudel PR, Kummari VC, Pandey B, Deoli NT, et al. An
624 overview of the facilities, activities, and developments at the University of North Texas
625 Ion Beam Modification and Analysis Laboratory (IBMAL). AIP Conf Proc [Internet].
626 2013 Jul 3;1544(1):11–8. Available from: <https://doi.org/10.1063/1.4813454>

627 37. Sharma M, Parashar M, Saini DK, Byers TA, Bowen C, Khanal MN, et al. In-Situ
628 Characterization Tools for Evaluating Radiation Tolerance and Elemental Migration in
629 Perovskites. In: 2024 IEEE 52nd Photovoltaic Specialist Conference (PVSC). 2024. p.
630 496–8.

631 38. Matej Mayer. SIMNRA User's Guide. 1997 Apr [cited 2024 Jul 22]; Available from:
632 <https://mam.home.ipp.mpg.de/Report%20IPP%209-113.pdf>

633 39. Ziegler JF, Ziegler MD, Biersack JP. SRIM – The stopping and range of ions in matter
634 (2010). Nucl Instrum Methods Phys Res B [Internet]. 2010;268(11):1818–23. Available
635 from: <https://www.sciencedirect.com/science/article/pii/S0168583X10001862>

636 40. Silva TF, Rodrigues CL, Mayer M, Moro M V, Trindade GF, Aguirre FR, et al.
637 MultiSIMNRA: A computational tool for self-consistent ion beam analysis using
638 SIMNRA. Nucl Instrum Methods Phys Res B [Internet]. 2016;371:86–9. Available
639 from: <https://www.sciencedirect.com/science/article/pii/S0168583X15010459>

640 41. Steele JA, Solano E, Hardy D, Dayton D, Ladd D, White K, et al. How to GIWAXS:
641 Grazing Incidence Wide Angle X-Ray Scattering Applied to Metal Halide Perovskite
642 Thin Films. Adv Energy Mater [Internet]. 2023 Jul 1;13(27):2300760. Available from:
643 <https://doi.org/10.1002/aenm.202300760>

644 42. Ashiotis G, Deschildre A, Nawaz Z, Wright JP, Karkoulis D, Picca FE, et al. The fast
645 azimuthal integration Python library: pyFAI. J Appl Crystallogr [Internet]. 2015
646 Apr;48(2):510–9. Available from: <https://doi.org/10.1107/S1600576715004306>

647